Joint Inference of Dominant Scatterer Locations and Motion Parameters of an Extended Target in High Range-Resolution Radar

A. De Freitas*, J. P. de Villiers*†, W. A. J. Nel†

*University of Pretoria, Pretoria, South Africa, allandefreitas1@gmail.com, pieter.devilliers@up.ac.za

†CSIR, Pretoria, South Africa, jdvilliers1@csir.co.za, wajnel@csir.co.za

This paper is a postprint of a paper submitted to and accepted for publication in IET Radar, Sonar and Navigation and is subject to Institution of Engineering and Technology Copyright. The copy of record is available at IET Digital Library

Abstract

A target of interest measured by a high range resolution radar may be modelled by multiple dominant points of reflections referred to as dominant scatterers. In this paper a non-linear state space setting is used to model the states and measurements of a target moving in the down- and cross-range dimensions. A resample-move particle filter with simulated annealing is successfully used to jointly infer the locations of the dominant scatterers and the motion parameters of the target. A novel technique for the initialization of the particle filter for the given application is presented. The location estimates of scatterers using the particle filter method are compared to those obtained using standard range-Doppler inverse synthetic aperture radar (ISAR) imaging when using the same radar returns for both cases. The particle filter infers the location of scatterers more accurately than range-Doppler ISAR processing, and the processing can be performed online as opposed to ISAR processing, which requires batching. It is relatively straightforward to extend the method to perform localisation and tracking of scatterers in three dimensions, whereas such an extension is challenging in range-Doppler ISAR processing. However, several challenges need be addressed to make this algorithm suitable for practical implementation and these challenges are discussed. This method may be used to obtain very accurate estimates of target state, which may in turn be used for accurate ISAR motion compensation. Given enough computing resources this algorithm may in future become the basis of a new radar target imaging scheme.

Index Terms

Particle filter, Extended target tracking, High range-resolution radar, ISAR.

I. INTRODUCTION

Radar systems utilise electromagnetic waves to detect and infer different characteristics of a target located within a specific region. This is performed through a two step process which includes the illumination of a specific region with electromagnetic waves, followed by the reception of any electromagnetic scatter which is reflected from objects in the region towards the radar system.When an electromagnetic wave is incident upon the surface of a target, it is scattered in a complex manner. The scattered wave directed towards the radar system from a target originates primarily from multiple individual reflection points, referred to as dominant scatterers [1].

A large variety of radar configurations exist [2]. The configuration of interest in this paper is of monostatic pulsed radar systems capable of achieving a high range-resolution (HRR), typically with a range resolution of less than a metre. HRR systems transmit high bandwidth waveforms to achieve the required range-resolution. Digital processing of the raw returns, observed by the radar, results in a discrete complex HRR profile. An HRR profile is a projection of the observable scatterers located in a three dimensional space to a single dimension, referred to as the range dimension, located along the radar line of sight [3]. Synthetic aperture radar (SAR) and inverse SAR (ISAR) images are projections of the observable scatterers located in a 3-D space to a 2-D image plane. A SAR/ISAR image can be generated from a sequence of HRR profiles that are obtained at different azimuth angles between the radar platform and the target [4]. This is achieved due to the effective rotational motion of the target and/or radar platform during the collection of HRR profiles. The ISAR technique directly relates to the approach advocated in this paper, since in ISAR processing the radar is assumed stationary while the target experiences relative rotational motion.

In ISAR processing, the target should ideally exhibit a constant rate of rotation around a fixed axis. In this case, and under the assumption that HRR profiles are collected over a period in which no migration of scatterers through resolution cells occur, an undistorted ISAR image can be obtained by performing a fast Fourier transform (FFT) on each range bin. When the motion of the target also consists of translational motion components, further preprocessing is required prior to the FFT on each range bin, to remove the effects thereof. Translational motion compensation focuses on removing the component of motion directed along the line of sight of the radar which jointly affects all the scatterers, whilst retaining the rotational motion. It is either carried out as a single step, or firstly as coarse range alignment followed by fine phase correction [5]. Conventional motion compensation algorithms generally assume that the rotational motion of the target is constrained to a 2-D plane during the interval in which the target is observed [6]. It has been found that many real world targets exhibit rotation in a 3-D plane, including aircraft undergoing fast manoeuvres [7] and ships at sea [8]. The presence of rotation in a 3-D plane may result in distorted ISAR images. It has also been found that ISAR images of targets subjected to a time-varying perturbed motion can lead to distortion in ISAR images [4].

The rotation induced by the target is essential in order to resolve the scatterers in the cross-range dimension[1]. However, the unknown complex motion of a target can result in severe distortion of ISAR images. Knowledge of the

[1]The cross-range is the direction perpendicular to the range dimension.

motion of the target would allow for the compensation of the distortive effects. Since ISAR is generally performed on uncooperative targets, a need to estimate the motion of a target prior to the generation of ISAR images is clearly evident.

The primary objective of this paper is to present a framework that is capable of tracking the locations of multiple dominant scatterers in space and motion parameters of an extended target that is observed by a monostatic pulsed HRR radar. It is assumed that the target is uncooperative and hence the only available measurements are the noisy 1-D HRR profiles obtained from the processing of the radar data. Essentially, it is required to infer 2-D or 3-D positions from convoluted 1-D data.

Several different approaches have been applied to the tracking of extended targets, with applications including the tracking of multiple extended targets and the joint estimation of the extent of the target as well as its motion parameters [9], [10]. An assumption made in these papers is that the observation sources are not fixed upon the target. This assumption is made due to the possibility of occlusions and large changes in the location of measurements sources. This is a realistic situation for HRR radar applications when measurements are collected over periods of time with large changes in the rotation angle. However, in our application it is assumed that the measurements are observed over periods of time in which small changes in the rotation angle are induced, as the dominant scatterers are persistent during such periods [1], [3], [11] and corresponds to measurement intervals used by ISAR processors based on the range-Doppler algorithm [12].

There are several approaches [13]–[15] which utilise the dominant scatterer assumption to infer scatterer locations and target motion parameters. The paper [13] addresses extended object tracking through the reconstruction of a multi-resolution problem by means of nonlinear optimisation, and is as such a non-Bayesian approach. In the paper by Hammarstrand et. al. [14], which appeared during the course of this research, the authors propose a Bayesian inference approach to scatterer localisation and tracking with application to radars on motor vehicles. The model is extensive and allows for the birth and death of scatterers, as well as dealing with clutter and unresolved measurements. However, sensor angle measurements are assumed to be available, in addition to range and range rate measurements as the result of a standard detection process. In contrast, in our paper, in addition to the range measurements, the phase changes of dominant scatterers are modelled explicitly and are used to determine the cross range position of scatterers over very small rotation angle changes of the extended target. Also, in our case, the targets are assumed to be at great distances and no angle measurements are available. In [15] a linear filter is utilised to track the dominant scatterers in range and Doppler prior to utilising a geometric inversion to obtain estimates for the location of the scatterers and the target motion.

In contrast to all the papers mentioned above, the approach in this paper is to jointly estimate and track the location of several dominant scatterers and the motion parameters of the extended target directly from the range line data. This will be performed through the use of a state space model and nonlinear Bayesian state estimation. The particle filter (PF) is a well documented sequential Monte Carlo method used for dynamic state estimation [16], [17], and was selected owing to its ability to deal with the non-linearities and non-Gaussian noise. The findings of this paper are extensions of the work presented in [18]. The work in [18] utilised a particle Markov Chain Monte

Carlo technique for the inference of static parameters. In this paper the state space model has been modified to allow parameters previously assumed as being static to be included in the dynamic state, resulting in the requirement of a simpler particle filter based algorithm. The inclusion of phase measurements from radar data allowed for a smaller angle range of rotation required to infer the target state. The novelty of this paper lies in the unique modelling of the state space system as well as the unique aspects relating to the implementation of the particle filter for this application.

II. MODELS

A target is represented as a set of points based on the assumption that a target consists of multiple dominant scatterers [1]. The points are located in a 2-dimensional space as illustrated by an example in Figure 1. A rigid body is assumed, in that it is assumed that scattering centres (scatterers) do not wander over the body of the target as the target moves, i.e. they are fixed to the target frame. Not all types of scatterers obey this assumption, and in Section II-A, the motion noise parameters can accommodate scatterers that do wander over the rigid body within limits. However, more accurate charaterisation of such wandering scatterers may be required in future investigations. This similar to the standard point target assumption in much of the ISAR radar literature [19].

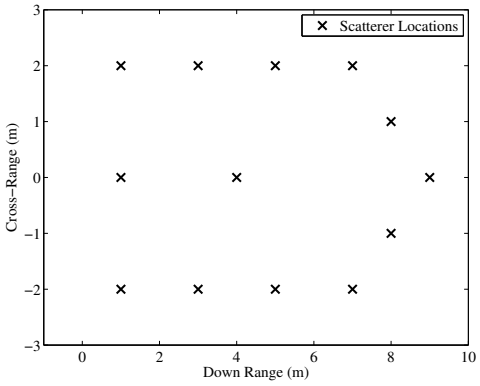

Fig. 1. Example of a target represented with dominant scatterers. Zero reference point of axes shifted to [10000,0].

It is assumed that the number of persistent scatterers M is fixed and constant during the observation period [20]. The expected approach would be to choose the M most dominant scatterers at the beginning of the simulation to track them throughout. This is not an entirely unreasonable assumption, since dominant scatterers may very well be persistent over the small target rotation angle which is required to localise scatterers and estimate the motion parameters. For an aerial target undertaking a rate 2 turn, this amounts to 0.64 seconds or 3.7 degrees of target rotation. The dimensions in Figure 1 are referred to as the down-range, $x^{\rightarrow}$, and cross-range, $x^{\perp}$, respectively. The radar is stationary and located at the origin of the co-ordinate system. The down-range dimension corresponds to the look direction of the radar. The cross-range dimension is perpendicular to the down-range dimension with the origin at the centroid of rotation of the target. In the three-dimensional case, there are two cross-range dimensions,

one which is tangential to the azimuth arc at the point passing through the target's centroid of rotation and the other is tangential to the elevation arc at the point passing through the target's centroid of rotation. For the purpose of comparing directly to standard 2-D ISAR techniques, a two-dimensional case is considered with a down-range and a single cross-range dimension. Figure 2 illustrates the down-range and cross-range dimensions relative to a target and the radar in a 2-D space. In this case, where the axis of rotation of the target does not lie in the azimuth or elevation planes, cross range is defined as follows. The radar ISAR image plane is defined by two unit vectors $(i_{\text{LOS}}, i_\Omega)$, where $i_\Omega = (\Omega \times i_{\text{LOS}})/|\Omega|$, and Ω represents the target rotation axis vector in 3-D space. The vector i_{LOS} represents the down-range dimension and the vector i_Ω defines the cross range dimension [21]. The projected rotation axis perpendicular to the image plane Ω_{eff} is given by $\Omega_{\text{eff}} = i_{\text{LOS}} \times (\Omega \times i_{\text{LOS}})$.

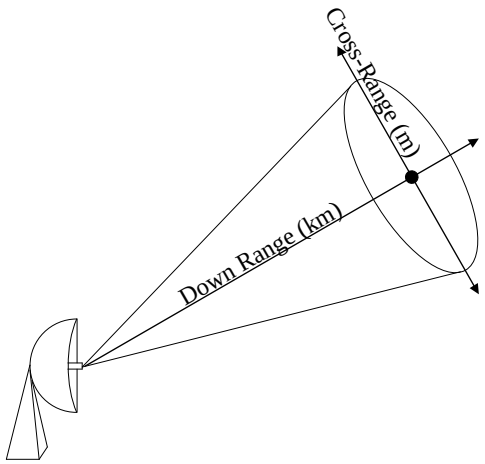

Fig. 2. Illustration of the axes relative to a target and the stationary radar.

Polar co-ordinates were selected for the representation of the location of the dominant scatterers to restrict non-linearities in the observation generation functions. The state vector is given by

$$\boldsymbol{x}_k = \left[\; r_{1,k}, \theta_{1,k}, \ldots, r_{M,k}, \theta_{M,k}, \omega_k \; \right], \tag{1}$$

where $r_{c,k}$ and $\theta_{c,k}$ represent the radius and angle of the scatterer $c = [1, \ldots, M]$ relative to the centroid of rotation and the cross-range axis respectively, and ω_k is the angular velocity of the target at discrete time instance k. An example of the state space representation of a random target consisting of two dominant scatterers is illustrated in Figure 3.

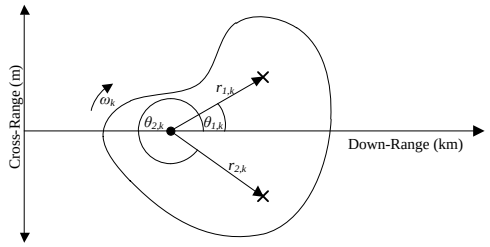

Fig. 3. Illustration of how the state vector relates to a target. The centre point on the target represents the centroid of rotation.

The true states of the target are hidden but are also related to a set of observations that are obtained at each time step. A state space model consists of models for the observations and the dynamics of the states. The state space model is represented by the following equations

$$\begin{aligned} \boldsymbol{x}_k &= a(\boldsymbol{x}_{k-1}, \boldsymbol{w}_k), \\ \boldsymbol{y}_k &= b(\boldsymbol{x}_k, \boldsymbol{v}_k), \end{aligned} \tag{2}$$

where $\boldsymbol{x}_k$ and $\boldsymbol{y}_k$ represent the states and observations at discrete time instant k respectively, $\boldsymbol{w}_k$ and $\boldsymbol{v}_k$ represent stochastic variables modelling the noise disturbances in the state dynamics and observations respectively, and $a(\cdot)$ and $b(\cdot)$ represent non-linear generation functions for the states and observations. A probabilistic equivalent to Eq. (2) is given by

$$\begin{aligned} \boldsymbol{x}_k &\sim f(\boldsymbol{x}_k|\boldsymbol{x}_{k-1}), \\ \boldsymbol{y}_k &\sim g(\boldsymbol{y}_k|\boldsymbol{x}_k). \end{aligned} \tag{3}$$

where $f(\cdot)$ is referred to as the state transitional density and $g(\cdot)$ is referred to as the observation density. The Markovian property is assumed for both models [17].

A. Motion Model

The motion of each dominant scatterer is directly related to the motion of the target. However, a stochastic variation between scatterers was also included. The rotational motion of the target was modelled with a discrete almost constant angular velocity random acceleration model [22]. The motion model for each state is given by

$$\begin{aligned} r_{c,k} &= r_{c,k-1} + p_{c,k}, \\ \theta_{c,k} &= \theta_{c,k-1} + \omega_{k-1}\Delta t + \frac{1}{2}\Delta t^2 q_k, \\ \omega_k &= \omega_{k-1} + \Delta t q_k, \end{aligned} \tag{4}$$

where Δt represents the constant time that is elapsed between discrete time steps, and $p_{c,k}$ and q_k represent zero-mean Gaussian random variables with respective standard deviations of σ_p and σ_q. Since the data is simulated, the dynamic noise parameters are chosen and hence σ_p and σ_q are place holders to model real world uncertainty, some aspects which are yet to be characterised. It is expected that in a real world problem, motion uncertainty may enter in several forms, which may include turbulence in the case of an air target, as well as the fact that the real

scattering centres are not necessarily stationary on a rigid body. The random walk property which accompanies the evolution of $r_{c,k}$ is to account for the fact that real scattering centres move over time, especially on curved surfaces of the target. The choice of a almost constant angular velocity model for ω_k is simply a first order choice and is a standard model for Newtonian dynamics in the absence of significant accelerations.

B. Observation Model

The dominant scatterers were modelled with the point scatterer model which assigns a specific amplitude and phase to each dominant scatterer. The signal received from the target consists of the complex summation of all scatterers. There are several different waveforms and signal processing techniques which can produce an HRR profile [2]. A general expression for an HRR profile is represented by

$$s_o(t) = \sum_i \sigma_{\mathrm{RCS}_i} e^{\frac{-j4\pi f_0 R_i}{c}} f\left(t - \frac{2R_i}{c}\right) + e_n, \tag{5}$$

where i represents the scatterer index, σ_{RCS_i} represents the amplitude of the returned signal based on the radar cross section for scatterer i, $f(t)$ represents the point spread function, which is related to the bandwidth, B, of the transmit waveform used by the radar, f_0 represents the radar operating carrier frequency, c represents the speed of light, e_n represents complex noise which is induced during the signal processing of the radar measurements and is directly related to the signal-to-noise ratio (SNR), and R_i represents the distance between the radar and scatterer i which is assumed fixed during the collection of data for a single HRR profile. The resolution of a range cell is given by

$$\Delta R_{cell} = \kappa \frac{c}{2B}, \tag{6}$$

where κ represents a scaling factor which takes into consideration any signal processing operations which degrade the resolution, such as windowing [2]. The complex returns of all the scatterers which are located within a single range resolution cell constructively or destructively interfere to result in a combined response. In this paper the stepped frequency waveform (SFW) approach described in [1] was utilised to obtain an HRR profile, with the addition of a zero mean Gaussian noise on the in-phase and quadrature channels of the radar receiver at a specific SNR, prior to windowing and performing the inverse Fourier transform. This resulted in a discrete form of Equation (5).

The observations extracted from each HRR profile include the range and phase of each dominant scatterer. In addition to the extracted observations, the PF requires the stochastic relationship as described by Equation (3). However, in this application, this relationship varies, depending on the type of scatterers residing in each range cell of the HRR profile. All possible scenarios can be described by one of three categories [23]. The categories include when a range bin contains a large number of small scatterers with no dominant scatterers; when a range bin contains a number of small scatterers with a single dominant scatterer present; and when a range bin contains a number of small scatterers with multiple dominant scatterers present. The observation models and application of tracking dominant scatterers in this paper assumes the category which consists of at most a single dominant

scatterer within a range cell at any given time. Methods to deal with the case of multiple dominant scatterers in a range cell are discussed later.

The first processing step performed is the thresholding of the magnitude of the HRR profile. This is performed in order to isolate the peaks related to dominant scatterers. The threshold level is manually set according to the SNR in the simulation. The discrete ranges corresponding to the peaks in the magnitude of the HRR profile are then obtained through a basic peak detection algorithm. The corresponding range obtained from the peaks represent the range to each dominant scatterer.

1) Range Measurement: This measurement describes the physical distance between the radar and the scatterer. In terms of the hidden states, the generation function for each observation is modeled as

$$R_{c,k} = \sqrt{\left(r_{c,k}\cos(\theta_{c,k}) + x_{\times}^{\rightarrow}\right)^2 + \left(r_{c,k}\sin(\theta_{c,k})\right)^2} + v_k, \tag{7}$$

where $x_{\times}^{\rightarrow}$ represents the location of the centroid of rotation in the down range, and v_k is a zero-mean Gaussian random variable. Although in reality $x_{\times}^{\rightarrow}$ is dynamic and unknown, here it is assumed to be static and known. The reason for this assumption is based on the fact that the scatterers' state information in the range and cross-range dimensions is derived from the rotation of the rigid body. Adding motion to the centroid of rotation will simply add an equal translational component to the motion of all the scatterers. Hence the special case of a rotating rigid body with a stationary centroid of rotation is considered here. In a more realistic setting where $x_{\times}^{\rightarrow}$ has motion, the state of $x_{\times}^{\rightarrow}$ can be modelled by augmenting $\boldsymbol{x}_k$ with the state variables of $x_{\times}^{\rightarrow}$ and specifying an appropriate motion model for these state variables. Since the motion of the target centroid $x_{\times}^{\rightarrow}$ is severely constrained on the time scale which is considered here, a simple almost constant velocity motion model [24] would suffice. Furthermore, motion compensation algorithms exist which could remove the velocity component of $x_{\times}^{\rightarrow}$ an can be found in [5], [25]–[27] and [28]. The method presented in this paper can be extended using the state augmentation approach or any of these motion compensation algorithms, but falls beyond the scope of this paper.

Note that the cross range origin always corresponds to the centroid of rotation in the cross range dimension, and the locations and motion of scatterers are always relative to this origin. Hence the absolute location of the cross range origin does not need to be known or estimated. The only constraint is that all scatters need to be inside the angular extent of the radar beam.

2) Phase Measurement: The range to each dominant scatterer is the only information that can be extracted from the magnitude of the HRR profile and was the only information extracted in the previous work presented in [18]. However, additional information can be extracted from the complex HRR profile by finding the phase at the extracted range to each dominant scatterer. The absolute phase measurement is a highly accurate range measurement which suffers from very large degrees of ambiguity. The progression of phase, referred to as the delta phase, is the difference in absolute phase of each scatterer between two consecutive HRR profiles. The delta phase measurement is still ambiguous on the interval $[-\pi;\pi]$ but is substantially less likely to wrap around the range in comparison with the absolute phase. The generation function for the delta phase of each scatterer is given by

$$\Delta\phi_{c,k} = \frac{4\pi\Delta R_{c,k}}{\lambda} + e_{\phi}, \tag{8}$$

where

$$\Delta R_{c,k} = \sqrt{\left(r_{c,k}\cos(\theta_{c,k}) + x_{\times}^{\rightarrow}\right)^2 + \left(r_{c,k}\sin(\theta_{c,k})\right)^2}$$
$$-\sqrt{\left(r_{c,k-1}\cos(\theta_{c,k-1}) + x_{\times}^{\rightarrow}\right)^2 + \left(r_{c,k-1}\sin(\theta_{c,k-1})\right)^2},$$

λ is the wavelength of the transmitted signal, and e_ϕ is a noise term which corresponds to the effects of the complex noise term in Eq. (5) on the delta phase measurement of each scatterer. The effect of this noise on the delta phase, e_ϕ, was modeled with the von Mises distribution, also commonly known as the circular Gaussian distribution [29], due to the circular interval that the delta phase is defined on. The Von Mises functional form was verified by fitting the model to samples generated by simulation. The probability density function of the Von Mises distribution is given by

$$p(\theta|\theta_0, m) = \frac{1}{2\pi I_0(m)}\exp\{m\cos(\theta - \theta_0)\} \qquad \theta \in [0, 2\pi) \tag{9}$$

where $I_0(m)$ is the zeroth-order Bessel function of the first kind, θ_0 is the mean, and m is the concentration parameter. The mean and concentration parameter are analogous to the mean and inverse variance of a univariate Gaussian respectively. In this application the mean was equal to 0 and the concentration parameter was found to be dependent on the SNR in the radar simulator.

When compared with the general expression typically used to describe the observation generation equation in Eq. (2), the generation function in Eq. (8) is dependent on the state at the previous time step which violates the Markovian property of the state space model [17]. The state vector was augmented with the states from the previous time step to prevent the violation of the Markovian property, since it is a fundamental property in the development of the state estimation algorithm. The observation vector is thus finally given by

$$\boldsymbol{y}_k = \left[\ R_{1,k}, \Delta\phi_{1,k}, \ldots, R_{M,k}, \Delta\phi_{M,k}\ \right]. \tag{10}$$

It is required to perform data association in order to correctly label the extracted measurements. Data association is not the focus of this study, and classical global nearest neighbour data association [30] was selected to be used in our application. It was implemented using the auction algorithm. Any of the more advanced data association techniques may also be used and these include multiple hypothesis tracking [31], joint probabilistic data association [30] and probabilistic multiple hypothesis tracking [32].

III. Dynamic State Estimation

Utilising a Bayesian framework, the tracking density of interest is the filtering distribution, $p(\boldsymbol{x}_k|\boldsymbol{y}_{1:k})$. A closed form expression for the filtering density is not tractable due to non-linearities and non-Gaussian noise present in the state space model.

A. The Particle Filter

Particle filtering is a technique which allows for the acquisition of a discrete estimate for the filtering distribution,

$$\hat{p}(\boldsymbol{x}_k|\boldsymbol{y}_{1:k}) = \frac{1}{N}\sum_{i=1}^{N}\delta^i_{\boldsymbol{X}_k}(\boldsymbol{x}_k), \tag{11}$$

where $\boldsymbol{X}_k^i \sim p(\boldsymbol{x}_k|\boldsymbol{y}_{1:k})$ and N represents the total number of samples selected for the representation. The PF achieves this discrete representation through a sequential algorithm based on the application of sequential importance sampling [17]. Initially, a set of N samples, also referred to as particles, are selected from the prior distribution. The particles are then weighted according to the first set of observations received. At each time step, two operations are performed. The particles are propagated through the state space by the application of a proposal distribution,

$$\boldsymbol{X}_k^i = q_k(\boldsymbol{x}_k|\boldsymbol{X}_{k-1}^i, \boldsymbol{y}_k), \tag{12}$$

where i represents the particle index, followed by the evaluation and normalisation of the importance weights,

$$w_k^i = w_{k-1}^i \frac{g(\boldsymbol{y}_k|\boldsymbol{X}_k^{\boldsymbol{i}}) f(\boldsymbol{X}_k^{\boldsymbol{i}}|\boldsymbol{X}_{k-1}^{\boldsymbol{i}})}{q_k(\boldsymbol{X}_k^{\boldsymbol{i}}|\boldsymbol{X}_{0:k-1}^{\boldsymbol{i}}, \boldsymbol{y}_{1:k})}, \tag{13}$$

$$\tilde{w}_k^i = \frac{w_k^i}{\sum_{j=1}^N w_k^j}. \tag{14}$$

This results in a discrete approximation for the filtering distribution at each time step, in the following form

$$\hat{p}(\boldsymbol{x}_k|\boldsymbol{y}_{1:k}) = \sum_i^N \tilde{w}_k^i \delta_{\boldsymbol{X}_k}^i(\boldsymbol{x}_k). \tag{15}$$

Although theoretically sound, this procedure is prone to weight degeneracy. Weight degeneracy occurs since the variance of the importance weights increases over time [33]. Essentially, a single particle will tend to have a normalised weight of 1, while the other particles' weights tend towards zero, resulting in a poor representation of the posterior distribution. To partially overcome weight degeneracy, the introduction of a resampling step after the evaluation of the importance weights was proposed [16], [34]. Through resampling, particles which contain higher weights are duplicated while particles with lower weights are eliminated, greatly alleviating the weight degeneracy problem. However, resampling may cause sample impoverishment, which is when particles with high weights are favoured to a large degree and can ultimately result in the entire set of particles being duplicates of a single particle. In order to prevent sample impoverishment, it has been proposed [35] to only perform resampling when weight degeneracy is severe. There are several measures of weight degeneracy that are utilised to determine when resampling should be performed. A commonly used measure is the effective sample size (ESS) [36],

$$\widehat{N}_{eff} = \frac{1}{\sum_i^N (\tilde{w}_k^i)^2}. \tag{16}$$

A value of 1 would indicate that all the probability mass is assigned to a single particle, indicating severe degeneracy, and conversely, the effective sample size approaches N when the weights tend to be uniformly spread among the particles. After resampling, the discrete approximation for the filtering distribution is given in Equation (11).

Two important practical design considerations in particle filtering are particle filter initialisation and the choice of proposal distribution.

1) Particle Filter Initialisation: It is imperative that the prior distribution is sufficiently defined in order to initialise the particles in highly probable regions in the state space. It is assumed that the target is non-cooperative. Hence, the prior information known about the target is limited to the maximum possible extent of the target, based on the radar operating parameters, and the assumption that the motion model accurately describes the motion of the

target. Observing two HRR data points results in two range measurements and a single delta phase measurement. It is proposed that these observations could aid in obtaining a more accurate particle initialisation. The mapping between the state space and the observation space is represented by the observation generation functions in Equations (7) and (8). However, this is not a unique mapping and any observation, when mapped to the state space, can result in many different locations in the state space. This is further influenced by the noise of the observation process. The aim is to populate particles in all the regions of the state space which could result in the observations received. The first step is to perturb the observations by the noise which is associated with the observation generation functions. This may move the observations possibly towards observations that represent the mapping of the true states to the observation space. After this step it is assumed that the noise terms in the observation generation functions are removed, resulting in a noiseless mapping between the state space and observation space,

$$\begin{aligned} R_{c,k} &= \sqrt{\left(r_{c,k}\cos(\theta_{c,k}) + x_{\times}^{\rightarrow}\right)^2 + \left(r_{c,k}\sin(\theta_{c,k})\right)^2} \\ \Delta\phi_{c,k} &= \frac{4\pi\Delta R_{c,k}}{\lambda}, \end{aligned} \tag{17}$$

where $\Delta R_{c,k} = R_{c,k} - R_{c,k-1}$. However, these relationships do not describe a mapping between the observation space and the state representing the angular velocity of the target. A relationship was derived to relate the observations to the angular velocity dimension in the state space. Firstly, the delta phase observation is related to the difference in range for each scatterer through

$$\Delta R_c = \frac{\Delta\phi_c\lambda}{4\pi}. \tag{18}$$

The difference in range is related to the radial velocity of the scatterer through

$$v_{r,c} = \frac{\Delta R_c}{\Delta t}. \tag{19}$$

The radial velocity is related to the angular velocity of the overall target and the down- and cross-range location of the specific scatterer through

$$\begin{aligned} v_{r,c} &= v\cos\theta_{a,c} \\ v_{r,c} &= \omega r_c\cos\theta_{a,c} \\ v_{r,c} &\approx \omega\sqrt{\left(x_c^{\rightarrow} - x_{\times}\right)^2 + {x_c^{\perp}}^2} \\ &\quad \cos\left(\frac{\pi}{2} + \tan^{-1}\left(\frac{x_c^{\perp}}{x_c^{\rightarrow} - x_{\times}}\right)\right), \end{aligned} \tag{20}$$

where $\theta_{a,c}$ represents the angle between the radar and the velocity vector of scatterer c, and is not to be confused with the angles in the state space. The further away a dominant scatterer is from the centroid of rotation, the larger the distance that the scatterer moves given the same angular velocity. By making the angular velocity the subject of the formula in Equation (20), and substituting the maximum cross-range location for any scatterer and the range observation as the down-range location results in a minimum possible angular velocity for the target

$$\omega_{\min,c} = \frac{v_{r,c}}{\sqrt{\left(R_c - x_{\times}\right)^2 + {x_{\max}^{\perp}}^2}\cos\left(\frac{\pi}{2} + \tan^{-1}\left(\frac{x_{\max}^{\perp}}{R_c - x_{\times}}\right)\right)}. \tag{21}$$

Finding the maximum of the minimum angular velocities determined for each dominant scatterer results in the minimum angular velocity of the target for the specific particle due to the rigid body assumption,

$$\omega_{\min} = \max_{c} \omega_{\min,c}. \tag{22}$$

The relationship between the range observation and the down-range and cross-range locations of each scatterer is given by

$$R_c = \sqrt{x_c^{\rightarrow 2} + x_c^{\perp 2}}. \tag{23}$$

Making the down-range location in Equation (23) the subject of the formula, and substituting into Equation (20) result in

$$\begin{aligned} v_{r,c} = \omega \sqrt{\left(\sqrt{R_c^2 - x_c^{\perp 2}} - x_\times\right)^2 + x_c^{\perp 2}} \\ \cos\left(\frac{\pi}{2} + \tan^{-1}\left(\frac{x_c^{\perp}}{\sqrt{R_c^2 - x_c^{\perp 2}} - x_\times}\right)\right). \end{aligned} \tag{24}$$

After determining the minimum angular velocity for the particle, the angular velocity state is initialised according to

$$\omega \sim U(\omega_{\min}, \omega_{\max}), \tag{25}$$

where $\omega_{\max}$ is the maximum angular velocity fixed in simulation. The sampled angular velocity is then substituted into Equation (24). With the knowledge of the radial velocity and range for each scatterer, the only unknown variable in the equation is the cross-range location. Once the cross-range location was inferred for each scatterer, the value was substituted into Equation (23) to obtain a corresponding down-range location. The down-range and cross-range locations for each scatterer were then converted into the polar domain. This process was repeated for the initialisation of each particle.

2) Choice of Proposal Distribution: Theoretically, there is an infinite number of possible choices for the proposal distribution, as the only criteria for the proposal distribution is that its support must include that of the filtering distribution [37]. However, the optimal proposal distribution is the distribution which minimises the variance of the importance weights [38],

$$q_k(\boldsymbol{x}_k|\boldsymbol{X}_{k-1}^i, \boldsymbol{y}_k) = p(\boldsymbol{x}_k|\boldsymbol{X}_{k-1}^i, \boldsymbol{y}_k). \tag{26}$$

Substituting this proposal distribution into Equation (13) results in the following iterative importance weight update

$$w_k^i \propto w_{k-1}^i p(\boldsymbol{y}_k|\boldsymbol{X}_{k-1}^i) = w_{k-1}^i \int g(\boldsymbol{y}_k|\boldsymbol{x}_k) f(\boldsymbol{x}_k|\boldsymbol{X}_{k-1}^i) d\boldsymbol{x}_k. \tag{27}$$

However, sampling from this proposal distribution and solving the integral in Equation (27) are not possible with the exception of very few state space models. Alternatives to implementing the optimal proposal distribution include using sub-optimal proposal distributions and using approximations of the optimal proposal distribution. A popular sub-optimal choice for the proposal distribution is the state transitional density [16], $q_k(\boldsymbol{x}_k|\boldsymbol{X}_{k-1}^i, \boldsymbol{y}_k) = f(\boldsymbol{x}_k|\boldsymbol{X}_{k-1}^i)$.

This selection of proposal distribution is commonly referred to as the bootstrap particle filter (BPF). Subsequently, the importance weights are then updated according to

$$w_k^i = w_{k-1}^i g(\boldsymbol{y}_k | \boldsymbol{X}_k^i). \tag{28}$$

The BPF has the advantage of reducing the computational complexity required for the calculation of the importance weights. However this choice of proposal distribution fails to take the current observation into account when propagating the particles through the state space.

There are also several approaches which approximate the optimal proposal distribution. One of the most notable approaches is referred to as the unscented particle filter (UPF) [39]. The UPF approximates the optimal proposal distribution with a Gaussian distribution. The UPF achieves this approximation through the implementation of the unscented Kalman filter (UKF). The UKF is based upon the scaled unscented transformation (SUT), which is essentially a method for determining the statistics of a random variable which undergoes a non-linear transformation.

The UPF has been shown to perform well in applications in which the likelihood density is peaked relative to the state transition density as illustrated in Figure 4.

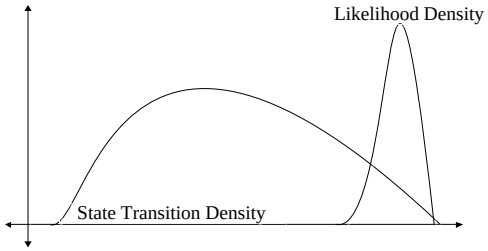

Fig. 4. Illustration of the likelihood density in terms of the state space and state transition density.

This is due to the fact that the proposal distribution takes the latest observation into account. This allows the filter to move the particles into areas which result in high likelihoods. However, the problem faced in this specific application, is that the state transition density is peaked relative to the prior distribution. The prior distribution has a relatively large extent, in the order of metres, due to the limited information of the target available during filter initialisation. The state transition density has a relatively small extent, in the order of millimetres for the radar parameters utilised, due to the small amount of motion incurred between the collection of HRR profiles. The limited motion between HRR profiles is required to prevent delta phase wrap. This results in the degeneration of the estimates obtained from the UPF. Unlike the BPF, the weight for each particle in the UPF is dependent on the state transition density, as noted by Equation (13). The mismatch between the prior distribution and state transition density results in the weights obtaining a value of zero due to particles being moved to locations in the state space where the state transition density approaches zero. As such the BPF was the selected technique.

B. Annealed MCMC step

The resample-move method of Gilks and Berzuini [40] together with simulated annealing [41] are used to mitigate the degenerative nature of this inference problem. This method consists of adding a single Markov Chain Monte Carlo (MCMC) Metropolis Hastings step after particle filter resampling. The proposal distribution for the MCMC step was chosen as a Gaussian with 1cm standard deviation in the down-range and a 30cm standard deviation in the cross-range. A move in the angular velocity dimension of the state vector was found not to be necessary. The weight ratio of the proposed particle state $\bar{\boldsymbol{X}}_k^i$ to the original particle state $\boldsymbol{X}_k^i$ is used to determine if the proposed move is accepted. The proposed particle state is accepted with probability

$$P_a(i,k) = \min\left(1, \frac{\bar{w}_k^i}{w_k^i}\right), \tag{29}$$

where $\bar{w}_k^i$ is the calculated weight of the proposed particle state. As motivated in [40] each selected particle, before moving is approximately distributed according to the posterior distribution. Hence after the move, the particle remains approximately from the posterior distribution, and as such the typical MCMC burn-in period is not required. Simulated annealing was effected as follows. The BPF is initialised with a 10 fold increase in both the variance for the delta phase and range observations to obtain the results in this paper. The annealing schedule is implemented such that the variances are decreased at equal intervals on a logarithmic scale such that the true observation variance is reached by the time half of the HRR profiles were processed. This means that during processing of the second half on the HRR profiles, filtering is performed using actual variances on the state dynamics and observations as generated by the radar and target simulator. Annealing allows for particles to initially explore the state space than would otherwise be possible, roughly finding the modes of the true posterior, while as real time progresses, the particles are increasingly concentrated around the support of the very peaked true posterior distribution.

IV. Results

The simulated target is a disc with a radius of 7m containing six dominant scatterers that are randomly located within a quarter of the disc. Figure 5 illustrates the starting location, final location and trajectory for each of the dominant scatterers on the disc. The parameters of the target and its motion are listed in Table I. The parameters relate to an air target undergoing a rate 2 turn. The parameters σ_p and σ_q were chosen such that the resulting scatterer motion does not induce phase wrap in the delta phase measurement, such as observed in real HRR data of a dominant scatterer depicted in Figure 11. The simulated radar operating parameters are summarized in Table II. These are based on a practical radar measurement experimental setup used for target classification research and is based at the CSIR in South Africa. The SNR values given are after HRR processing (i.e. with signal processing gain). The marginal filtering distribution for the state representing the angular velocity for all time steps is illustrated in Figure 6. The intensity of gray indicates the density of particles in that region of the state space. The states corresponding to the range and angle of each of the scatterers were converted to the down-range and cross-range dimensions. Figure 7 illustrates the log of the joint marginal filtering distribution for the final time step for the

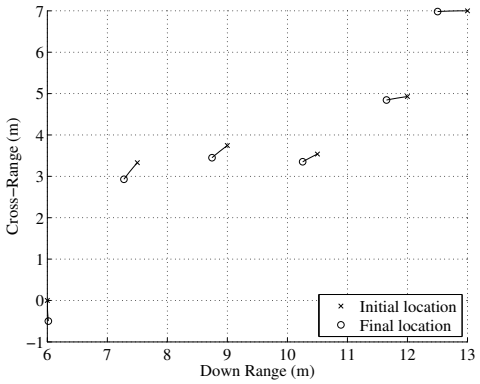

Fig. 5. Trajectory of a random target consisting of 6 dominant scatterers. Zero reference point of axes shifted to [10000,0].

TABLE I

DEFINING PARAMETERS OF THE RANDOM TARGET.

Parameter	**Parameter Value**
Number of dominant scatterers	6
Angular velocity (ω_r)	0.1 rad/s
Centroid of rotation co-ordinates($[x_\times, 0]$)	$[10013, 0]$ m
Motion model std. deviations ($[\sigma_q, \sigma_p]$)	$[1 \times 10^{-3}\text{m}, 1 \times 10^{-9}\text{m.s}^{-2}]$
Total time elapsed	0.64 s
Time difference between points (Δt)	6.4 ms

down-range and cross-range location of the dominant scatterers. As can be expected, the distribution is more diffuse in the cross-range dimension than the range dimension, since the cross-range locations are not observed directly, but are inferred from the motion of the target over several HRR profiles. This is contrasted to the equivalent ISAR image generated through standard range-Doppler processing of the HRR profiles in Figure 8. Here the classical

TABLE II

SFW BASED HRR RADAR SIMULATOR PARAMETER VALUES.

Radar Parameter	**Parameter Value**
Step Frequency (Δf)	10 MHz
Number of Pulses per HRR profile (n)	64
Centre Frequency (f_0)	10 GHz
Effective Pulse Repetition Frequency (PRF)	10 KHz
Signal-to-noise Ratio (SNR)	20dB (10dB, 15dB in Table III)
Range resolution	23.42 cm

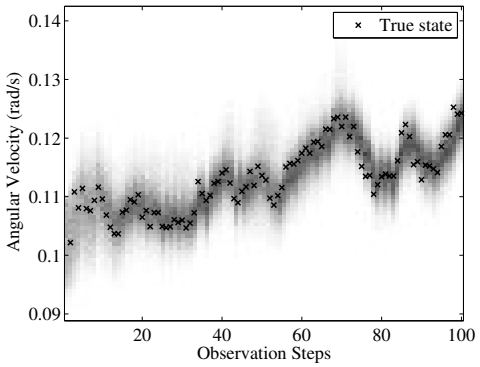

Fig. 6. The marginal filtering distribution for the angular velocity.

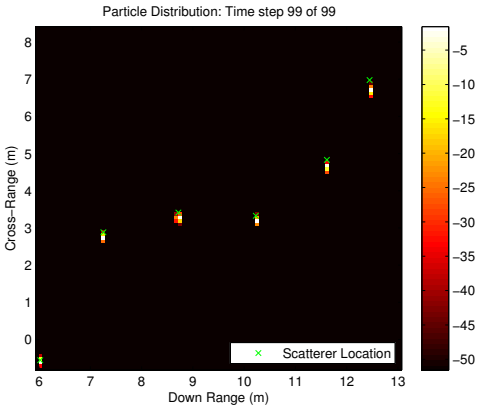

Fig. 7. The log marginal filtering distribution for the states corresponding to the locations of the dominant scatterers after processing all HRRs. Zero reference point of axes shifted to [10000,0]m.

motion compensation by Haywood [42] and the dominant scatterer algorithm (DSA) [43] auto focusing methods were used as a baseline for comparison. The root mean-square-error (RMSE) determined from the converted state estimates over 50 simulation runs is given in Table III. In the down-range dimension, the PF method attains a location accuracy in the order of 1/10th of the wavelength of the centre frequency. The accuracy in the cross range dimension is about 4 times the wavelength of the centre frequency. Note that the target rotation rate is estimated jointly with the scatterer positions, and hence the location accuracy does not necessarily need to be in the order of 1/10 of the carrier frequency wavelength to obtain a useful result.

The effect of decreasing the number of dominant scatterers being tracked was investigated by eliminating dominant scatterers 1 and 3 to 6 of the target illustrated in Figure 5. The resulting marginal filtering distribution for the state representing the angular velocity for all time steps is illustrated in Figure 9. Hence, considering more scatterers in the estimation process has the effect of reducing the uncertainty in the target motion estimates.

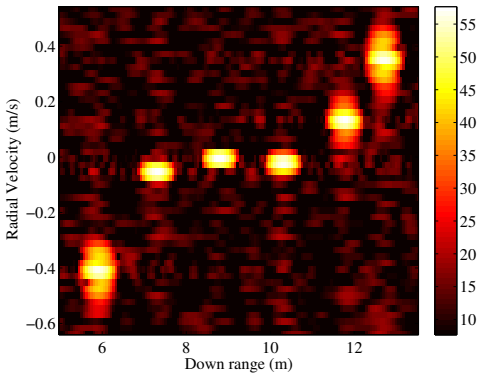

Fig. 8. ISAR image produced through standard Doppler processing techniques. Zero reference point of axes shifted to [10000,0].

TABLE III

RMSE CALCULATED OVER 50 INDEPENDENT MONTE CARLO RUNS.

State (SNR = 10 dB)	$x_1^{\rightarrow}$ (mm)	$x_1^{\perp}$ (mm)	$x_2^{\rightarrow}$ (mm)	$x_2^{\perp}$ (mm)	$x_3^{\rightarrow}$ (mm)	$x_3^{\perp}$ (mm)	$x_4^{\rightarrow}$(mm)
RMSE	4.5	243.7	3.8	295	3.4	278.8	10.4
σ_{RMSE}	0.6	5.1	0.9	70	0.6	91	0.5
State (SNR = 10 dB)	$x_4^{\perp}$ (mm)	$x_5^{\rightarrow}$ (mm)	$x_5^{\perp}$ (mm)	$x_6^{\rightarrow}$ (mm)	$x_6^{\perp}$ (mm)	ω (mrad/s)	
RMSE	223.7	7.9	320.04	4.1	494.9	8.4	
σ_{RMSE}	99.2	0.5	154.2	0.8	200.5	3.5	
State (SNR = 15 dB)	$x_1^{\rightarrow}$ (mm)	$x_1^{\perp}$ (mm)	$x_2^{\rightarrow}$ (mm)	$x_2^{\perp}$ (mm)	$x_3^{\rightarrow}$ (mm)	$x_3^{\perp}$ (mm)	$x_4^{\rightarrow}$(mm)
RMSE	1.3	57.9	2.1	150.6	3.1	192.5	1.6
σ_{RMSE}	0.3	2.8	0.4	57.0	0.2	63.3	0.2
State (SNR = 15 dB)	$x_4^{\perp}$ (mm)	$x_5^{\rightarrow}$ (mm)	$x_5^{\perp}$ (mm)	$x_6^{\rightarrow}$ (mm)	$x_6^{\perp}$ (mm)	ω (mrad/s)	
RMSE	157.2	2	228.1	1.8	318.7	5.3	
σ_{RMSE}	70.8	0.3	98.4	0.3	141.5	1.5	
State (SNR = 20 dB)	$x_1^{\rightarrow}$ (mm)	$x_1^{\perp}$ (mm)	$x_2^{\rightarrow}$ (mm)	$x_2^{\perp}$ (mm)	$x_3^{\rightarrow}$ (mm)	$x_3^{\perp}$ (mm)	$x_4^{\rightarrow}$(mm)
RMSE	2.1	81.2	2.3	115.4	2.2	141.5	2.1
σ_{RMSE}	1.4	43.5	0.9	57.5	1.0	76.9	1.1
State (SNR = 20 dB)	$x_4^{\perp}$ (mm)	$x_5^{\rightarrow}$ (mm)	$x_5^{\perp}$ (mm)	$x_6^{\rightarrow}$ (mm)	$x_6^{\perp}$ (mm)	ω (mrad/s)	
RMSE	122.4	1.8	146.4	1.7	190.5	4.5	
σ_{RMSE}	62.2	0.9	74.6	0.9	102.7	1.6	

V. DISCUSSION

Table III shows that PF scatterer position estimate accuracies over 50 Monte Carlo runs are typically in the order of millimetres in the down-range dimension and decimetres in the cross-range dimension. When the SNR is degraded from 20dB to 10dB, there is not a significant degradation in location accuracies. At poor SNR values, the limitation becomes correct data association, since noise peaks in the HRR profile start to cross the threshold. In such

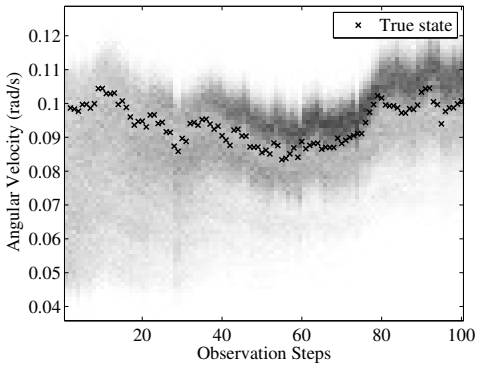

Fig. 9. The marginal filtering distribution for the angular velocity when only two dominant scatterers are observed.

cases the GNN association algorithm will need to distinguish between noise and scatterer return threshold crossings. If dominant scatterers can be accurately identified at the start of the tracking window, the GNN data association does maintain these even if occasional noise threshold crossings do occur. These threshold crossings typically occur at SNR values between 5dB and 10dB. In addition to unwanted threshold crossings, dominant scatterer returns may also fail to cross the threshold, owing to scatterers being suppressed by destructive interference with noise. These cases are currently not handled by PF and should be addressed in future work. However if the SNR deteriorates enough (below 5dB), the data association will fail, and consequently also the PF method. This could be mitigated to some extent by utilising advanced data association methods such as joint probabilistic data association or multiple hypothesis tracking.

Comparing Figure 7 and 8 illustrates the difference in results obtained with the PF approach and the range-Doppler ISAR processing equivalent. The particles in the PF represent the most likely hypothesis for the true state given the noisy observations. The PF location estimates are more accurate than the ISAR image, and the latter also contains unwanted artifacts owing to Fourier processing. Table IV highlights the differences between ISAR and the PF approach presented. ISAR makes use of pre-processing methods to compensate for the motion of the target and Doppler processing to form an image. The method proposed in this work uses a parametric model of the motion and observation of the scatterers on the target. This incorporates prior information about how the motion of the scatterers is constrained and how they are observed. Hence, higher location accuracies can be expected than with ISAR, since a prior understanding of the process which generates the data is implicitly incorporated in the model.

ISAR processing is not dependent on the number of scatterers present in an HRR profile. In contrast, the state dimensionality of the particle filter increases with the number of scatterers, hence increasing the computational complexity of the filter. This results in a constraint on the number of scatterers that can be processed. The PF approach requires data association, and in this case, global nearest neighbour data association is used. Data association may be altogether averted if random finite set tracking is used [44], although this would entail an entirely new study. ISAR processing does not directly produce an image with a cross-range dimension and further

TABLE IV
A COMPARISON BETWEEN ISAR AND THE PF APPROACH.

	ISAR	**PF Approach**
Type of scatterers processed	All	Dominant Only
Computational complexity	Low	High
State dimension dependent	N/A	Yes
Dependent on data association	N/A	Yes
Motion parameter estimates	No	Yes
Cross-range directly available	No	Yes
Type of processing	Batch	Batch/Sequential
Extension of results to a 3-D space	Challenging	Straightforward

processing would be required to convert the radial velocity dimension into the cross-range dimension. The PF approach can process new data sequentially on-line, whereas the ISAR algorithm requires the data to be batched for off-line processing. Finally, the PF approach can be extended to tracking scatterers in three dimensions, through the addition of an extra spatial dimension for each of the scatterers and a corresponding modification of the motion model to accommodate motion in three dimensions. Although this is to be verified in future work, it is expected that this method will again outperform 3-dimensional ISAR, owing to the use of parametric models for the motion and observation equations. This improvement will incur computational complexity owing to the fact the more parameters would have to be estimated. Even though there are certain cases for which the motion of the target based on the HRR observation is ambiguous, the particle filter, if implemented correctly should maintain a representation of this ambiguity. A particular challenge of current 3-D ISAR methods is related to the compounding of errors in the estimation of rotation axis and rate [45], [46]. It is the opinion of the authors that the model based approach followed here also has a better chance than existing 3-D ISAR methods at addressing phase errors owing to interfering scatters, and this is explored in the next section. If a suitable technique can be found to visualise the particle clouds of the PF in three dimensions, and enough scatterers can be considered, this method may in future form the basis of a new radar imaging scheme.

This algorithm was originally developed with air targets in mind and hence the effect of clutter was not considered. In the case of surface targets, such as the example presented in the next section, it is expected that the algorithm would reject clutter effectively, owing to the peaked nature of the likelihood. Hence particles associated with scatterers that do not adhere to the expected motion of the target (such as clutter) are expected to receive very low weights.

VI. FUTURE INVESTIGATION

Future research will focus on removing simplifying assumptions and extending the framework to handle real world data (RWD). Preliminary studies to meet these ends have been conducted and are presented in this section.

Unlike the ideal dominant scatterer based model simulations utilized in this paper, HRR profiles based on RWD may be influenced by several additional factors, such as returns from weak scatterers and additional scattering mechanisms. In order to address these factors, several pre-processing steps and adjustments to the framework presented may be required. An important step in the framework presented is the extraction of observations of the dominant scatterers from the HRR profiles. All measurements above a specific threshold in the magnitude of the HRR profile were assumed to be considered as dominant scatterers. This may not necessarily be valid for RWD. The reason for this is due to the assumption that two dominant scatterers are not located within the same range bin. However, this may occur in RWD. When two or more dominant scatterers are located in the same range bin, the complex returns from the scatterers are combined into a single result for the given range bin. This may result in constructive or destructive interference which can lead to an increase or decrease in the amplitude of the magnitude of the HRR profile, and a change in the delta phase observed. By analysing RWD it is noted that range bins which consist of only a single dominant scatterer have a relatively consistent delta phase when compared to range bins which consist of multiple scatterers. This is illustrated in Figures 10 to 12 below. Figure 10 consists of the magnitude of a set of range aligned HRR profiles obtained from a maritime vessel [47]. Analysing Figure 10, it is clear that a dominant scatterer is located within the region of range bin 37. The delta phase for range bin 37 is illustrated in Figure 11. To contrast, the delta phase for range bin 31, which may consist of multiple scatterers, is illustrated in Figure 12. The variability of the delta phase can be used to distinguish between range bins which consist of single dominant scatterers or multiple dominant scatterers by monitoring the delta phase prior to tracking. As an extension, it was found that the shape of the probability distribution of the delta phase of a specific range bin is directly related to the types of scatterers located within the range bin. Hence, characterising the probability distribution of the delta phase in a range bin prior to initialisation and tracking could aid in identifying range bins consisting of dominant scatterers. Further, after the filter is initialized to track a set of dominant scatterers, additional steps can be taken to identify new dominant scatterers as well as to identify when dominant scatterers may merge into a single range bin. Future investigations would therefore be aimed at extending the framework to support a variable dimension state space, along the lines of [14].

VII. Acknowledgments

The authors would like to acknowledge the King Abdulaziz City for Science and Technology (KACST) in the Kingdom of Saudi Arabia and the Council for Scientific and Industrial Research (CSIR) in South Africa for funding this research.

References

[1] Wehner, D.R.: High Resolution Radar (Norwood, MA: Artech House, 1995), 2nd edn.

[2] Richards, M.A., Scheer, J.A., and Holm, W.A.: Principles of Modern Radar, Volume I - Basic Principles (SciTech Publishing, 2010)

[3] Xing, M., Bao, Z., and Pei, B.: 'Properties of high-resolution range profiles', Optical Engineering, Feb 2002, 41(2), pp. 493–504

[4] Wong, S.: 'High Range Resolution Profiles as Motion-Invariant Features for Moving Ground Targets Identification in SAR-Based Automatic Target Recognition', IEEE Trans. Aerosp. Electron. Syst., July 2009, 45(3), pp. 1017 –1039

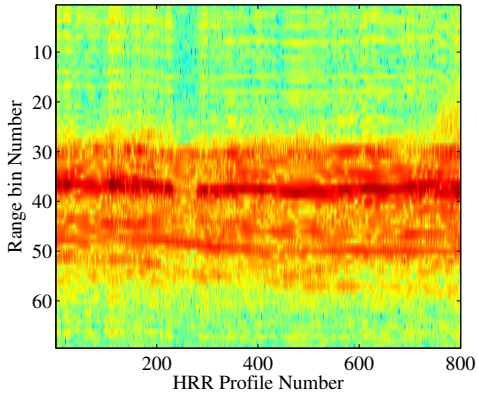

Fig. 10. Set of magnitude of HRR profiles obtained from RWD.

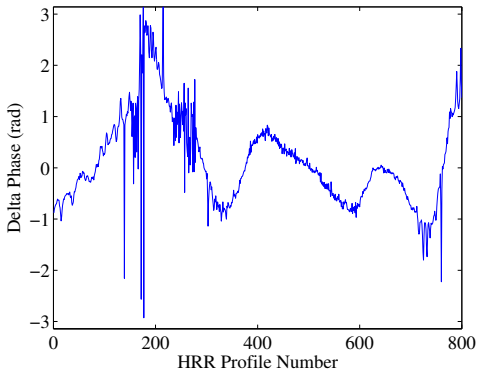

Fig. 11. The delta phase for range bin 37 of Figure 10.

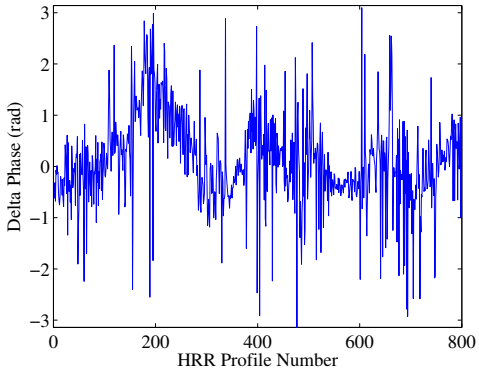

Fig. 12. The delta phase for range bin 31 of Figure 10.

[5] Nel, W., Giusti, E., Martorella, M., *et al.*: 'A time domain phase-gradient based ISAR autofocus algorithm', in '2011 IEEE CIE Int. Conf. Radar', vol. 1 (2011), pp. 541 –544

[6] Li, J., Ling, H., and Chen, V.: 'An algorithm to detect the presence of 3D target motion from ISAR data', Multidim. Syst. Sign. Proc., July 2003, 14(1), pp. 223–240

[7] Chen, V.C. and Miceli, W.J.: 'Effect of roll, pitch, and yaw motions on ISAR imaging', Proc. SPIE 3810, Radar Proc. Tech. App. IV, Sept 1999, pp. 149–158

[8] Nel, W., Stanton, D., and Gaffar, M.: 'Detecting 3-D rotational motion and extracting target information from the principal component analysis of scatterer range histories', in 'Int. Radar Conf. - Surveilance for a Safer World', (2009), pp. 1–6

[9] Baum, M. and Hanebeck, U.D.: 'Extended Object Tracking Based on Set-Theoretic and Stochastic Fusion', IEEE Trans. Aerosp. Electron. Syst., Oct 2012, 48(4), pp. 3103 –3115

[10] Granstrom, K. and Orguner, U.: 'A phd Filter for Tracking Multiple Extended Targets Using Random Matrices', IEEE Trans. Signal Process, Nov 2012, 60(11), pp. 5657 –5671

[11] Ballard, B., Darron, C., Gostin, L., *et al.*: 'Dominant scatterer identification testing with an integrated X-band radar system', IEEE Aerosp. Electron. Syst. Mag., Feb 2002, 17(2), pp. 21 –26

[12] Ausherman, D.A., Kozma, A., Walker, J.L., *et al.*: 'Developments in Radar Imaging', IEEE Trans. Aerosp. Electron. Syst., July 1984, AES-20(4), pp. 363 –400

[13] Zhang, Y., Xiao, Y., and Hu, S.: '3D motion and geometric information system of single-antenna radar based on incomplete 1D range data', J. Systems Eng. & Electronics, June 2011, 22(3), pp. 412–420

[14] Hammarstrand, L., Lundgren, M., and Svensson, L.: 'Adaptive Radar Sensor Model for Tracking Structured Extended Objects', IEEE Trans. Aerosp. Electron. Syst., July 2012, 48(3), pp. 1975 –1995

[15] Shapo, B., Stuff, M., Kreucher, C., *et al.*: 'Detection and tracking of prominent scatterers in SAR data', in 'Proc. SPIE', vol. 8394 (2012)

[16] Gordon, N., Salmond, D., and Smith, A.: 'Novel approach to nonlinear/non-Gaussian Bayesian state estimation', IEE Proc. F Radar and Signal Proc., April 1993, 140(2), pp. 107–113

[17] Cappe, O., Godsill, S., and Moulines, E.: 'An Overview of Existing Methods and Recent Advances in Sequential Monte Carlo', Proc. IEEE, May 2007, 95(5), pp. 899 –924

[18] De Freitas, A. and De Villiers, J.: 'Multiple scatterer tracking in high range resolution radar', in '15th Int. Conf. Information Fusion', (2012), pp. 1683–1688

[19] Stoyle, P.: 'Point scatterers in radar imaging', in 'Proc. SPIE', vol. 3462 (1998)

[20] Ballard, B., Darron, C., Gostin, L., *et al.*: 'Dominant scatterer identification testing with an integrated X-band radar system', in 'Proc. IEEE Radar Conf.', (2001), pp. 18 –22

[21] Martorella, M.: 'Novel approach for ISAR image cross-range scaling', Aerospace and Electronic Systems, IEEE Transactions on, January 2008, 44(1), pp. 281–294

[22] Bar-Shalom, Y., Li, X.R., and Kirubarajan, T.: Estimation with Applications to Tracking and Navigation (Wiley-Interscience, 2001), 1st edn.

[23] Du, L., Liu, H., Bao, Z., *et al.*: 'A two-distribution compounded statistical model for Radar HRRP target recognition', IEEE Trans. Signal Process., June 2006, 54(6), pp. 2226 – 2238

[24] Blackman, S.S.: Multiple-Target Tracking with Radar Applications (Norwood, MA: Artech House, 1986)

[25] Thompson, P., Wahl, D.E., Eichel, P.H., *et al.*: Spotlight-Mode Synthetic Aperture Radar: A Signal Processing Approach (Kluwer Academic Publishers, Norwell, MA, USA, 1996)

[26] Yau, D., Berry, P.E., and Haywood, B.: 'Eigenspace-based motion compensation for ISAR target imaging', EURASIP J. Appl. Signal Process., Jan 2006, 2006, pp. 134–134

[27] Yuan, C. and Casasent, D.: 'Composite filters for inverse synthetic aperture radar classification of small ships', Optical Engineering, 2002, 41(1), pp. 94–104

[28] Berizzi, F., Dalle Mese, E., and Martorella, M.: 'Performance analysis of a contrast-based ISAR autofocusing algorithm', in 'Radar Conference, 2002. Proceedings of the IEEE', (2002), pp. 200–205

[29] Bishop, C.M.: Pattern Recognition and Machine Learning (Information Science and Statistics) (Springer-Verlag New York, Inc., 2006)

[30] Karlsson, R. and Gustafsson, F.: 'Monte Carlo data association for multiple target tracking', in 'IEE Target Tracking: Alg. & App.', vol. 1 (2001), pp. 13/1–13/5

[31] Reid, D.: 'An algorithm for tracking multiple targets', IEEE Trans. Auto. Control, Dec 1979, 24(6), pp. 843–854

[32] Gauvrit, H., Le Cadre, J.P., and Jauffret, C.: 'A formulation of multitarget tracking as an incomplete data problem', IEEE Trans. Aerosp. Electron. Syst., Oct 1997, 33(4), pp. 1242–1257

[33] Kong, A., Liu, J.S., and Wong, W.H.: 'Sequential Imputations and Bayesian Missing Data Problems', J. Amer. Statist. Assoc., March 1994, 89(425), pp. 278–288

[34] Rubin, D.B.: 'A noniterative sampling/importance resampling alternative to the data augmentation algorithm for creating a few imputations when fractions of missing information are modest: the SIR algorithm', J. Amer. Statist. Assoc., June 1987, 82(398), pp. 543–546

[35] Arulampalam, M., Maskell, S., Gordon, N., *et al.*: 'A tutorial on particle filters for online nonlinear/non-Gaussian Bayesian tracking', IEEE Trans. Signal Proc., Feb 2002, 50(2), pp. 174 –188

[36] Liu, J.S.: Monte Carlo Strategies in Scientific Computing (New York: Springer, 2008)

[37] Doucet, A., Gordon, N., and Krishnamurthy, V.: 'Particle filters for state estimation of jump Markov linear systems', IEEE Trans. Signal Proc., March 2001, 49(3), pp. 613 –624

[38] Doucet, A., Godsill, S., and Andrieu, C.: 'On sequential Monte Carlo sampling methods for Bayesian filtering', Statistics & Computing, July 2000, 10(3), pp. 197–208

[39] van der Merwe, R., de Freitas, N., Doucet, A., *et al.*: 'The Unscented Particle Filter', in 'Advances Neural Inf. Proc. Systems 13', (2001)

[40] Gilks, W.R. and Berzuini, C.: 'Following a moving target – Monte Carlo inference for dynamic Bayesian models', Journal of the Royal Statistical Society: Series B (Statistical Methodology), Jan 2001, 63(1), pp. 127–146

[41] Andrieu, C., de Freitas, N., Doucet, A., *et al.*: 'An introduction to mcmc for machine learning', Machine Learning, 2003, 50(1-2), pp. 5–43

[42] Haywood, B. and Evans, R.J.: 'Motion compensation for ISAR imaging', in 'Proc. of ASSPA '89', (1989), pp. 113–117

[43] Steinberg, B.D.: 'Microwave imaging of aircraft', in 'Proc. IEEE', vol. 76 (1988), pp. 1578–1592

[44] Vo, B.N., Singh, S., and Doucet, A.: 'Sequential Monte Carlo methods for multitarget filtering with random finite sets', Aerospace and Electronic Systems, IEEE Transactions on, Oct 2005, 41(4), pp. 1224–1245

[45] Stuff, M.A., Sanchez, P., and Biancalana, M.: 'Extraction of Three-Dimensional Motion and Geometric Invariants from Range Dependent Signals', Multidimensional Systems and Signal Processing, 2003, 14, pp. 161–181

[46] Lord, R., Nel, W., and Abdul Gaffar, M.: 'Investigation of 3-D RCS image formation of ships using ISAR', in 'Proc. European Conference on Synthetic Aperture Radar, EUSAR 2006', (Dresden, Germany, 2006)

[47] Gaffar, M.Y.A.: 'Maritime Classification Processor: Report on TD0.5 alpha trial', Tech. Rep. 5840-HADAS-10017, CSIR, Jan 2011